Microstructural Evolution of Type 304 and 316 Stainless Steels under Neutron Irradiation at LWR Relevant Conditions

L. Tan, 1,4 R.E. Stoller, K.G. Field, Y. Yang, H. Nam, D. Morgan, B.D. Wirth, M.N. Gussev, and J.T. Busby

1.—Oak Ridge National Laboratory, Oak Ridge, TN, USA. 2.—University of Wisconsin, Madison, WI, USA. 3.—University of Tennessee, Knoxville, TN, USA. 4.—e-mail: tanl@ornl.gov

Life extension of light water reactors will expose austenitic internal core components to irradiation damage levels beyond 100 displacements per atom (dpa), leading to profound microstructural evolution and consequent degradation of macroscopic properties. Microstructural evolution, including Frank loops, cavities, precipitates, and segregation at boundaries and the resultant radiation hardening in type 304 and 316 stainless steel (SS) variants were studied in this work via experimental characterization and multiple simulation methods. Experimental data for up to 40 heats of type 304SS and 316SS variants irradiated in different reactors to 0.6–120 dpa at 275–375°C were generated from this work or collected from literature reports. These experimental data were then combined with models of Frank loop and cavity evolution, computational thermodynamics and precipitation, and ab initio and rate theory integrated radiation-induced segregation models to provide insights into microstructural evolution and degradation at higher doses.

INTRODUCTION

Life extension of current light water reactors (LWRs) is a potential method of meeting escalating needs for carbon-free energy. The reliability of critical component materials is the limiting factor governing reliable, economical extension of the operating lives of LWRs with an original license period of 40 years in the United States of America for an additional 20 years or longer. Irradiation-assisted stress corrosion cracking (IASCC) has been identified as one of the major radiation-induced degradation phenomena in internal core structural components fabricated using austenitic stainless steels (SS) and located near nuclear fuel assemblies in LWRs. Radiation-induced changes in materials, including their microstructures, and resulting changes in macroscopic properties are considered the fundamental cause of IASCC.

The reported radiation-induced microstructural changes in austenitic SS core internals of LWRs primarily include a high density $(10^{22}-10^{23} \text{ m}^{-3})$ of Frank loops (< ~20 nm), precipitates (e.g., Ni/Si-rich γ' and G phases and carbides), and cavities, as well as chemical segregation at grain boundaries (GBs) and dislocations. Accumulated experimental data have shown some preliminary relationships between the effects of irradiation temperature and flux on radiation-induced microstructural changes, but completed systematic studies on the effect of alloying composition remain limited. The microstructural changes directly resulted in noticeable hardening, with as-irradiated yield stresses of up to ~1,000 MPa at room temperature accompanied by reductions in ductility (total elongation) to ~5% or less and reductions in fracture toughness to ~50 MPa \sqrt{m} from an initial ~400 MPa \sqrt{m} . Life extension to 60 years or longer will increase the irradiation damage levels for some components to more than 100 displacements per atom (dpa), posing significant challenges to the austenitic SS core

components. Therefore, understanding radiation-induced microstructural evolution is important to estimate component life, understand failure mechanism, and guide the development of advanced radiation-resistant materials.

To support the analysis of experimental observations and provide fundamental physical understanding and predictions, computational models were developed to study radiation-induced microstructural evolution. Among the different microstructural components, the modeling efforts in this work focused on the evolution of Frank loops and cavities, radiation-induced segregation (RIS), and precipitation. The defect evolution models provide a comprehensive description of the primary microstructural components in austenitic SS that evolve under irradiation, i.e., Frankfaulted dislocation loops, dislocation networks, and cavities (bubbles and voids). RIS describes the element redistribution in austenitic SS at random high-angle (HA) and coincidence site lattice (CSL, e.g., Σ 3) GBs under different irradiation conditions. Ab initio calculations for Ni-Cr and Ni-Fe were carried out to provide important parameters for RIS modeling. The precipitation modeling predicted the precipitate phases in the segregated compositions via an integrated computational thermodynamics and kinetics approach. Seamlessly integrating the evolving defect physics with the RIS and changes in the second-phase precipitates represents a true grand challenge within the radiation effects community, and the approaches described here represent the initial steps toward tackling this complex problem.

MATERIALS AND METHODS

Materials

This work investigated a set of type 304SS and 316SS variants. Many of the alloys were modified from a high-purity version of 304SS (alloy E) by altering the compositions of specific alloying elements—e.g., altering alloys F by reducing carbon and G, K, L, and P by adding Mo, Ni, (Ni+Cr), and (Mo+Hf), respectively. Additionally, two industrial heats of 304SS (alloys A and SW) and one industrial heat of 316SS (alloy B) were investigated together. Alloys G and P are also considered variants of 316SS because of their molybdenum additions. The alloy compositions are listed in Table 1. The alloying elements are in weight percentage (wt %) in this paper unless specifically noted. Different levels of cold work were applied to alloys B, E, F, and G. The other alloys were in an annealed condition, e.g., 1,050°C for 30 min followed by a water quench. Samples of the alloys were irradiated in the BOR-60 reactor at ~320°C for up to 47.1 dpa at a displacement rate of ~8×10⁻⁷ dpa/s.

Table 1	Allow co	mnositions	$(\mathbf{w}t^{0}/_{0})$ a	and the	investigated	camples
Taine I.	~ III) V L.	,,,,,,,,,,,,,,,,,,,,,,,,,,,,,,,,,,,,,,,	I W L 70 L a		HIVESHEARCH	Samuro

Tuble 1: 11110'y compositions (we 70') and the investigated samples										
Alloy ID	Remark	C	Mn	Si	Cr	Ni	Mo	Ti	Hf	Sample ID (dose, dpa)
	I., J. 204	0.022	1.02	0.56	10.05	10.0	0.52	0.02		AS13 (5,5), AS18
A	Ind. 304	0.023	1.82	0.30	19.95	10.8	0.53	0.02	_	(10.2), AS23 (47.1)
SW	Ind. 304	0.022	1.07	0.24	18.42	10.45	_	_	_	SW37 (4.4)
E	HP304	0.021	0.94	0.04	18.76	12.37	0.04	0.01	_	ES13 (11.8)
F	E-C	0.008	0.98	0.03	18.17	12.06	0.02	0.01	_	FS13 (9.1)
G	E+Mo	0.02	0.97	0.03	18.26	12.15	2.36	0.01		GS13 (11.8)
K	E+Ni	0.02	1	0.03	18.21	25.08	0.02	0.01	_	KS13 (9.6)
L	E+Ni+Cr	0.02	1.02	0.03	25.22	25.07	0.02	0.01	_	LS13 (9.1)
P	E+Mo+Hf	0.028	1.01	0.1	17.03	13.6	2.18	_	1.17	PS15 (9.6)
В	Ind. 316	0.056	1.13	0.73	16.84	10.54	2.25	0.01	_	BS13 (5.5), BS16 (10.2)

Note: Compared with levels of up to 0.29 Cu, 0.22 Co, 0.072 N, 0.023 P, and 0.022 S in the industrial alloys, the others are reported with <0.01 Cu, 0.01 Co, <0.0005 N, <0.01 P, and <0.007 S.

Experimental Methods

Irradiated microstructures were characterized using transmission electron microscopy (TEM) and scanning TEM (STEM) techniques on a Philips CM200 field-emission-gun TEM/STEM equipped with an EDAX energy-dispersive x-ray spectroscopy (EDS) detector. TEM discs of 3 mm diameter were extracted from the tab section of the irradiated tensile samples and mechanically thinned to less than ~100 μm, followed by electropolishing at −12°C in a methanol:sulfuric (7:1) solution using a Struers Tenupol polishing unit. To calculate the volumetric number densities of Frank loops, precipitates, and cavities in this work and the reviewed data, the TEM thin foil thickness was usually estimated by convergent beam electron diffraction or simply assumed to be nominally 100 nm. Microchemical investigations were conducted using 2-dimensional spectrum imaging techniques that employed the signal from the EDAX EDS detector with a region of interest of 50 by 50 nm with 25 by 25 pixels using a ~1.5 nm, 1 nA incident probe and a 1.5 s dwell time, unless otherwise noted. For all cases, quantification was completed using the Cliff-Lorimer quantification scheme, assuming normalized compositions based on those presented in Table 1.

Modeling and Simulation Methods

Cavities, Frank loops, and dislocation network

The primary microstructural code employed in this effort was developed on the basis of the investigator's previous research on materials in fast reactors with a radical revision and improvement of the cavity evolution model. A more detailed cavity nucleation and growth model based on cluster dynamics was developed and is described in ref. [8]. The new model is computationally more complex and provides a much more rigorous description of the physical phenomena involved in cavity nucleation. The cavity evolution component is integrated with a dislocation evolution component similar to that in the previous fast reactor model, and the complete model provides a comprehensive description of the primary microstructural components in austenitic SS that evolve under irradiation, i.e., cavities (bubbles and voids), Frank-faulted dislocation loops, and the dislocation network. The model explicitly accounts for the effects of helium that are introduced by nuclear transmutation but does not treat any other chemical effects, such as solute segregation.

Briefly, the code performs numerical integration of the master equations for the size distributions of gas bubbles and interstitial loops, coupled with equations for concentrations of the mobile species: single vacancies and interstitial atoms, gas atoms, and both dislocation loops and network dislocation densities. Cavity integration is performed in a phase space described by the number of vacancies and gas atoms in each cavity. The output includes the dose dependence of the cavity size distribution; the dislocation loop size distribution; and integral characteristics of the microstructure, such as bubble and loop densities, bubble and loop mean sizes, swelling, and network dislocation densities.

Radiation-induced segregation

A GB-interstitial-modified inverse Kirkendall (GiMIK) model was developed to account for RIS in austenitic Fe-Cr-Ni-Si alloys as a function of GB character. ¹¹ GiMIK is based on modified-inverse Kirkendall (MIK) models developed for Fe-Cr-Ni alloys by Allen et al., ¹² but it was modified to describe the boundary through an expression, based on work by Duh et al., to

describe boundary sink characteristics.¹³ Therefore, the concentration of point defects on the GB and the sink strength were modeled as functions of the GB misorientation angle, interfacial energy, and dislocation structure. Silicon segregation was modeled using the interstitial binding model, based on Lam and Wiedersich.^{14,15} Details for this GiMIK model implementation and parameter selection can be found in our recent work.¹¹

A parallel effort for RIS is to develop fundamental transport properties, such as diffusion coefficients of silicon in austenitic SS, from ab initio energetics. ¹⁶ This work combines transition state theory and multifrequency models to determine diffusion coefficients from ab initio energetics and then integrate them into mesoscale rate theory models to predict RIS. These ab initio—derived model parameters can be readily integrated in the GiMIK framework that has been developed.

Radiation-induced precipitation

Using the spatially independent thermokinetic software package MatCalc, 17, 18 the precipitation model attempts to incorporate full thermodynamics and kinetics modeling approaches to precipitate and second-phase evolution for alloy chemistry modified by RIS and having radiation-enhanced diffusion coefficients, but without any spatial dependence or any explicit radiation damage. 19 Within the MatCalc modeling approach, we modeled the equilibrium second-phase precipitate volume fractions along with the precipitation kinetics, assuming that the alloy compositions had changed because of RIS. We also incorporated the effects of neutron irradiation with regard to increasing the dislocation density and providing radiation-enhanced diffusivity of key alloying elements. 19 In this approach, we compared a base composition of 316SS with a modified composition corresponding to approximately 10 dpa of irradiation. By changing the alloy composition, as well as the nucleation density on dislocations and the constituent diffusivities, we can mimic the effects of irradiation within the MatCalc model of precipitation kinetics. The MatCalc model treats the kinetics of microstructural processes based on classical nucleation theory and on evolution equations for the radius and composition of each precipitate derived from the thermodynamic extremum principle. (Reference [20] provides details of the basic principles composing MatCalc).

Note that the thermodynamic calculation and the kinetic simulation are not spatially resolved and thus were not performed for all regions in the steel. Instead, we selected representative compositions that represent localized spatial regions, with different compositions from the bulk as a result of RIS. In such regions near strong defect sinks such as GBs, dislocations, or voids, RIS can provide a thermodynamic driving force for the formation of radiation-induced precipitations as locally stable phases. During the calculation and simulation, the thermodynamic and kinetic data for all phases, except γ' and G phases, were calculated from the MatCalc thermodynamic database "mc_fe" (version 2.003) and the MatCalc mobility database "mc_fe" (version 2.006), respectively. ²¹ The thermodynamic data for γ' were taken from the thermodynamic assessment of the Ni-Si-Ti system by Tokunaga et al. ²² The G phase was modeled as (Mn,Ti)6Ni₁₆Si₇ considering the solubility between Mn and Ti. The thermodynamic data for Mn₆Ni₁₆Si₇ and Ti₆Ni₁₆Si₇ were taken from the assessments of Hu et al. ²³ and Tokunaga et al., ²² respectively.

RESULTS AND DISCUSSION

Frank Loops

Frank loops have a primary contribution to radiation hardening, as compared with black spots and network dislocations at LWR-relevant temperatures. Radiation-induced Frank loops were often characterized using the rel-rod imaging technique with edge-on loops in dark-field TEM images. The statistically analyzed average sizes and densities of the loops observed in this work are plotted in Fig. 1 in solid circles. The literature data of similar alloys irradiated in different reactors at similar temperatures are included in Fig. 1 for comparison. C6,27,28,29,30,31,32,33,34,35,36 The literature data are primarily from BOR-60 sodium-cooled fast reactor and LWRs such as Tihange-1 and other pressurized water reactors (PWRs) in Japan and Ringhals-II and Barsebäck boiling water reactors. A few data from OSIRIS light-water experimental reactor and sodium-cooled EBR-II are also included. Type 304SS, 316SS, and 304SS alloyed with additional nickel and chromium are also differentiated in the figure by different colors. All the 316SS was subjected to cold work for a level of ~12–15%. In contrast, most of the 304SS was in solution-annealed condition.

Most of the data are from samples irradiated to doses <40 dpa. Stacking fault tetrahedral and partially dissociated dislocations were occasionally observed in the investigated samples and reported in some literature. They are not considered here because they did not influence the relrod loop analysis. Figure 1a shows a slight increase in average loop size with increasing dose and saturated in a range of ~5.7-12.5 nm (except for one abnormally large datum characterized in a 304SS with reduced sulfur content). As compared with the BOR-60 data, the data from LWRs generally exhibit loop size saturation at lower doses or larger loop size at the same dose. The average densities are on the order of 10^{22} to 10^{23} m⁻³, which increased to a maximum at ~6 dpa and then slightly decreased with increasing dose. The large data variations are likely attributable to the different irradiation temperatures (275–375°C), doses (0.6–120 dpa), dose rates, and alloy compositions. Additionally, difficulties in obtaining accurate and consistent sizes and densities were perceived during TEM characterization of Frank loops. Large deviations (~50%) from average sizes were usually observed for Frank loops. The large loops (a few tens of nanometers) may escape the thin foil during TEM specimen thinning, and glissile loops may escape to the free surfaces of the TEM specimens, resulting in reduced loop density and altered average size. The difficulty in selecting the right brightness threshold during image analysis often resulted in a variable cutoff for small loops, which reduced loop density and increased average size.

The effects of alloy chemistry on loop density and size were explored according to equivalent chromium and nickel contents and stacking fault energies (SFE). Equivalent chromium and nickel contents of the alloys were estimated using $Cr_{eq} = Cr + 2Si + 1.5Mo + 5V + 5.5Al + 1.75Nb + 1.5Ti + 0.75W$ and $Ni_{eq} = Ni + Co + 0.5Mn + 0.3Cu + 30C + 25N$, according to the Schaeffler diagram. The SFE of the alloys were estimated using SFE (mJ/m²) = -7.1 + 2.8Ni + 0.49Cr + 2.0Mo - 2.0Si + 0.75Mn - 5.7C - 24N. The SFE of alloys K and L were not calculated because their high chromium and nickel contents were beyond the applicable ranges of the equation. Additionally the SFE calculation for alloy P may not be as accurate as that for the other alloys because of the noticeable amount of Hf addition. Generally, noticeable correlations between loop size/density and alloy chemistry in terms of SFE and equivalent chromium and nickel were not observed. The variations in the experimental conditions of the samples may have suppressed the correlations. Figure 1c and 1d show the examples of the relationships between loop density and equivalent chromium, as well as SFE.

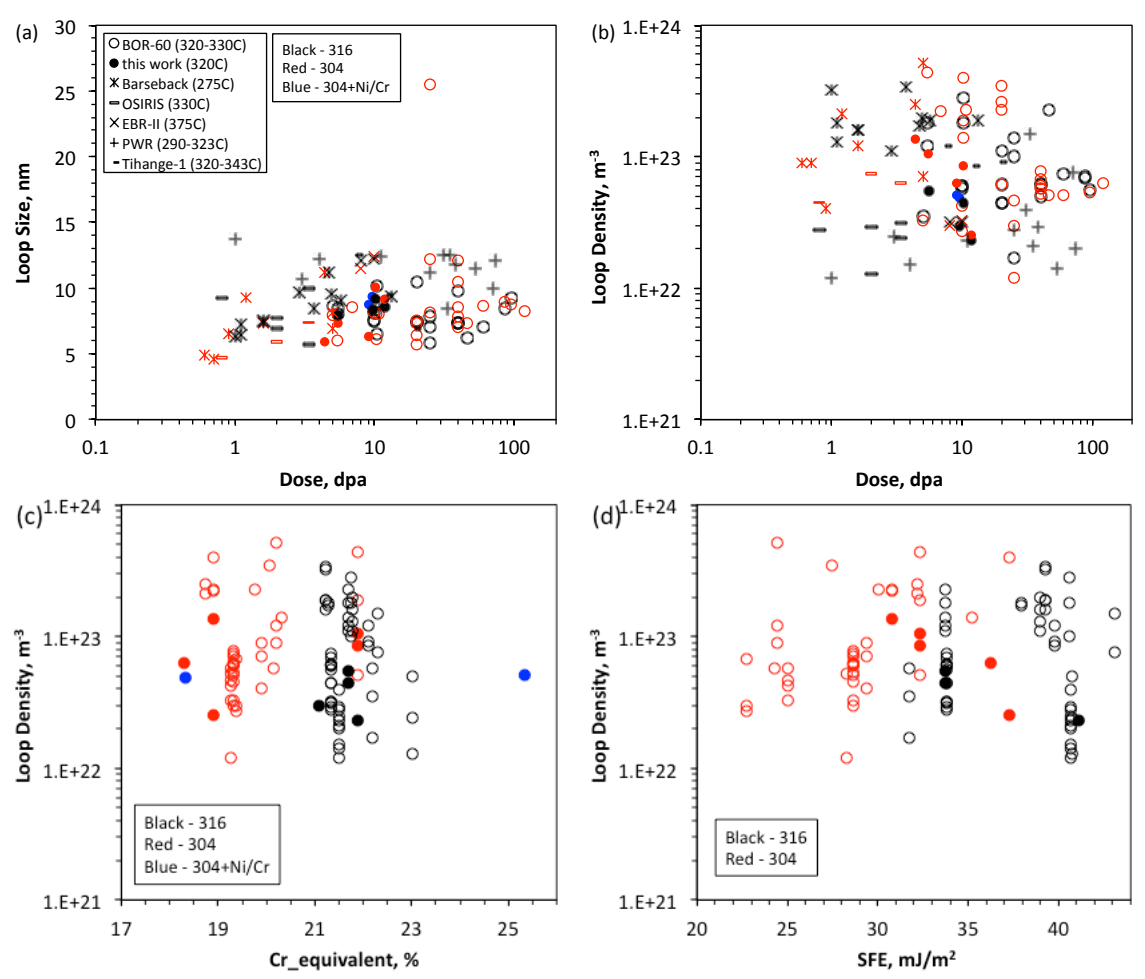


Fig. 1. Dose-dependent average loop (a) size and (b) density and the effects of (c) equivalent chromium content and (d) stacking fault energies on loop density.

Representative dislocation microstructures obtained with the current model are shown in Fig. 2 for irradiation temperatures of 275 and 300°C. The initial dislocation density was set to 5×10^{14} m⁻², which is a value typically observed at high doses in irradiated austenitic SS at somewhat higher temperatures. As a result, there is little change in this parameter over the course of the irradiation. A higher initial value may be more appropriate for heavily cold-worked material. The initial recovery of the dislocation network begins to be compensated for when the largest loops become unfaulted and become part of the network at about 1 dpa. The predicted Frank loop density at peak is near the lower limit of the data in Fig. 1b, but the mean size is similar, about 11 nm. The predicted loop density increases to a maximum at ~0.5 dpa and then slightly decreases with the increasing dose, which is consistent with the trend of the experimental data in Fig. 1b, but at about one order of magnitude lower in both the loop density and the dose reaching the maximum loop density. Adjustment and optimization of the initial parameters in this calculation model would provide more reliable prediction of the experimental data.

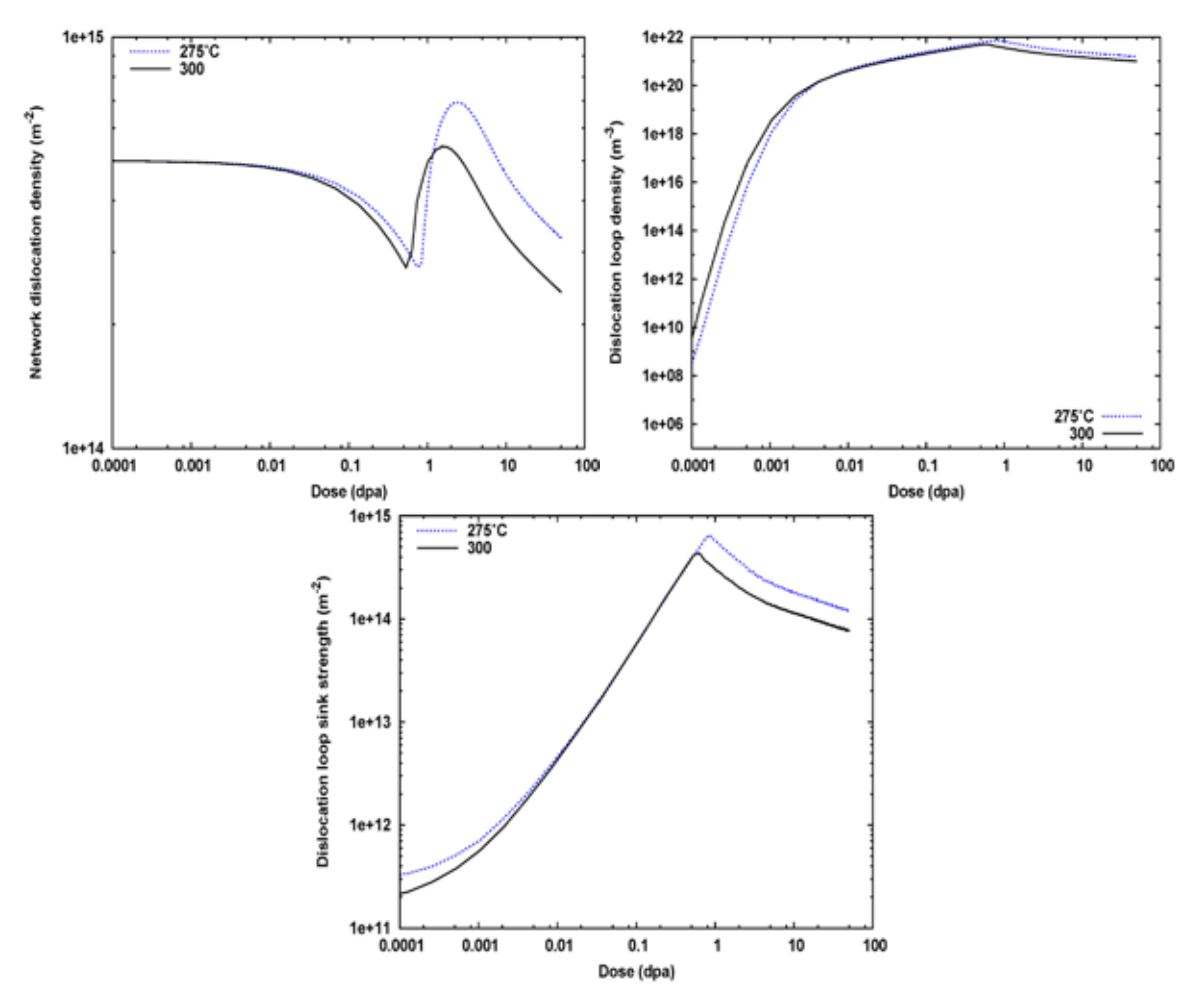


Fig. 2. Simulated dose dependence of dislocation structure at T=275 and 300°C for a representative austenitic stainless steel: (a) network dislocation density, (b) faulted dislocation loop density, and (c) faulted loop sink strength.

Cavities

Ultra-fine cavities were observed in some of the alloy samples in Table 1. The analyzed average cavity size, density, and volume fraction are plotted as a function of dose in Fig. 3, together with literature data for cold-worked 316SS and solution-annealed 304SS samples irradiated to 1–73 dpa at 290–375°C. ^{27,28,35,36,38} The swelling was estimated by the volume fraction of the cavities by assuming spherical shape of the cavities. The dominant cold-worked 316SS data show cavities of about 1–2 nm and densities on the order of 10^{23} m⁻³. The sample of alloy G (304SS+Mo) irradiated to ~11.8 dpa has the largest size (up to ~10 nm) and a low density on the order of 10^{20} m⁻³. The few 304SS data, primarily in a solution-annealed condition, yielded relatively larger cavity sizes and lower densities. Despite the variations in size and density, the cavity volume fractions (or swelling) of the cold-worked 316SS and solution-

annealed 304SS samples show good agreement. The swelling gradually increased to \sim 0.07% with increasing dose to \sim 70 dpa. Two cold-worked 316SS samples irradiated to 7.5 and 12.2 dpa at 333 and 343°C, respectively, showed exceptionally high swelling of \sim 0.2–0.24%. A solution-annealed 304SS sample irradiated at a higher temperature, 375°C, did not show such noticeable swelling. The detailed sample temperature history, dose rate, alloy chemistry, and possible other factors need to be analyzed to understand the discrepancy.

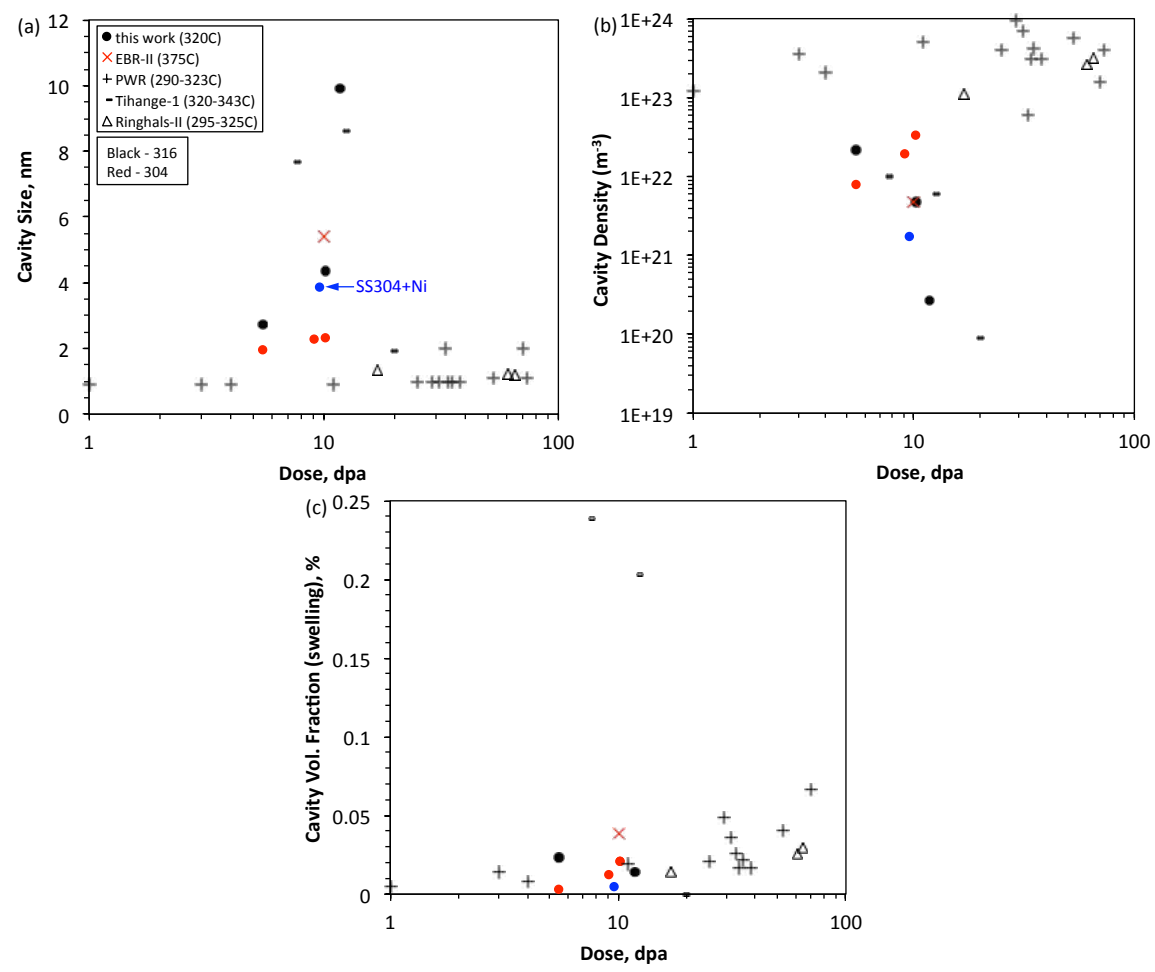


Fig. 3. Dose-dependent (a) size, (b) density, and (c) volume fraction of the cavities observed in this work (solid circles) and literature reports (open circles).

The dose dependence of the predicted cavity volume fraction or swelling is shown in Fig. 4 for irradiation temperatures of 275 and 300°C. The dose scale is again logarithmic to highlight the evolution. The effect of irradiation temperature is weak in this range. With the nominal set of material parameters used, the predicted dose dependent swelling gives the same trend but greater values than in the data shown in Fig. 3. Because of the coupling between the cavity and dislocation evolution, this result is likely related to the fact that the dislocation density is somewhat low, as discussed in reference to the results in Fig. 2. Further work is underway to investigate alternate parameterizations of the model to improve the comparisons between the predictions and available data. However, the results suggest that it may be reasonable to expect this material to have a tendency to swell even at these relatively low temperatures.

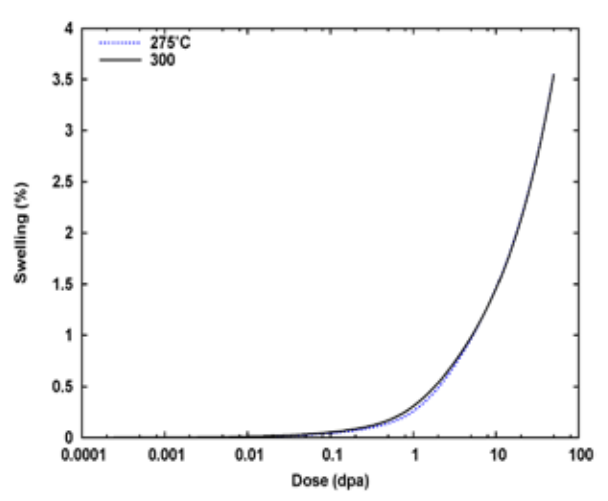


Fig. 4. Simulated dose dependence of predicted cavity swelling at T=275 and 300°C for representative austenitic stainless steel material parameters.

Radiation-Induced Segregation

RIS was observed in all alloys investigated (K, L, A, G, and E, Table 1). The effects of GB structure on RIS are illustrated in Fig. 5 (a) and (b), in which are plotted the experimentally measured and computationally simulated 1-dimensional segregation profiles for Cr, Ni, and Si for the random high-angle GBs (RHAGB) and CSL- Σ 3 GBs of alloy A for an irradiation dose of 47.1 dpa. Significant enrichment of Ni and Si and depletion of Cr were observed in the RHAGB, but no obvious segregation peaks were found for the CSL- Σ 3 GB. This plot shows that RIS at CSL- Σ 3 GBs tended to exhibit over a ~70% reduction in the RIS response over RHAGBs.

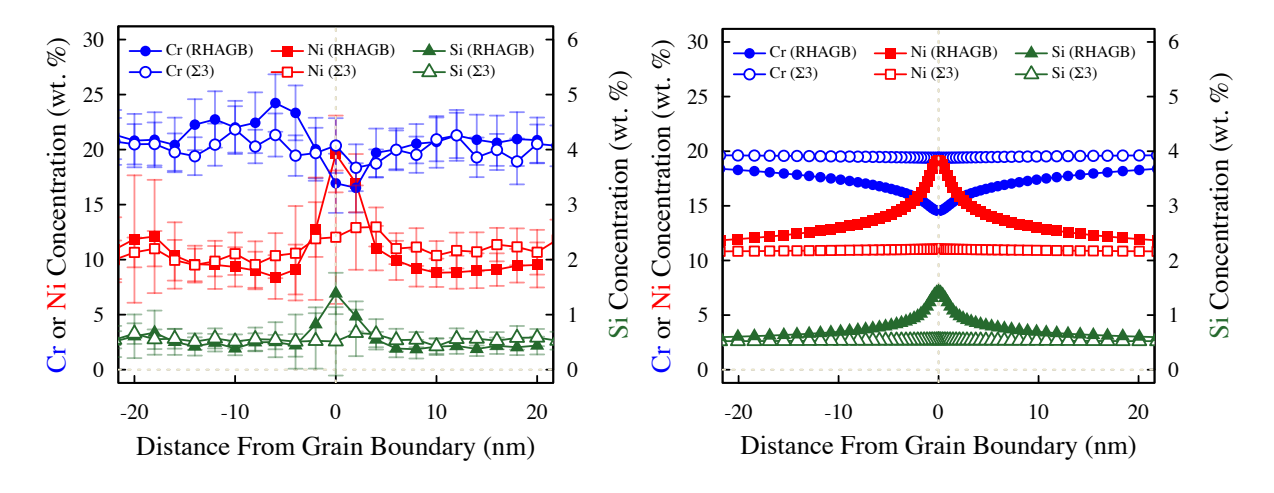


Fig. 5. One-dimensional concentration profiles from random high-angle and Σ 3 grain boundaries in the 47.1 dpa—irradiated specimen. (a) Experimental measurements (b) Simulation results.

The effect of dose on GB segregation is illustrated in Fig. 6, in which the changes in concentration of Cr, Ni, and Si at GBs in the investigated alloys are plotted against those reported in the literature at up to 70 dpa. Although it is not explicitly stated in the referenced

studies, based on the reported RIS responses, it is assumed that the data presented in Fig. 6 for literature values are based solely on the responses of RHAGBs. Within this study, several trends were observed. When a relatively constant dose (9–12 dpa) is considered, the highest observed RIS of nickel was in alloy K (304SS+Ni), whereas the lowest observed RIS of nickel was found in alloy G (304SS+Mo). Given this finding, care should be taken in interpreting the results, as the RIS values reported for alloy G are based on analyzing one GB because of the limited number of available GBs in that specimen for RIS analysis. The highest observed chromium depletion between 9 and 12 dpa was in alloy L (304SS+Cr). The resulting variations in the RIS response based on bulk alloy composition clearly show the dependencies between composition and RIS for irradiated 304/316SS. The only alloy investigated for dose trends was alloy A. As seen in Fig. 6, the chromium depletion and nickel and silicon enrichment at the GB increased with increasing dose. Values found in this study for RHAGBs fell within the scatter band of the data presented in the literature for similar radiation doses (dpa). Some variation in presented data is expected, as RIS studies are known to be sensitive to analysis factors such as GB tilt, specimen foil thickness, and quantification techniques.^{39,40} The simulation results represent the calculated segregation values for alloy A and clearly fall within the scatter band range of the literature values.

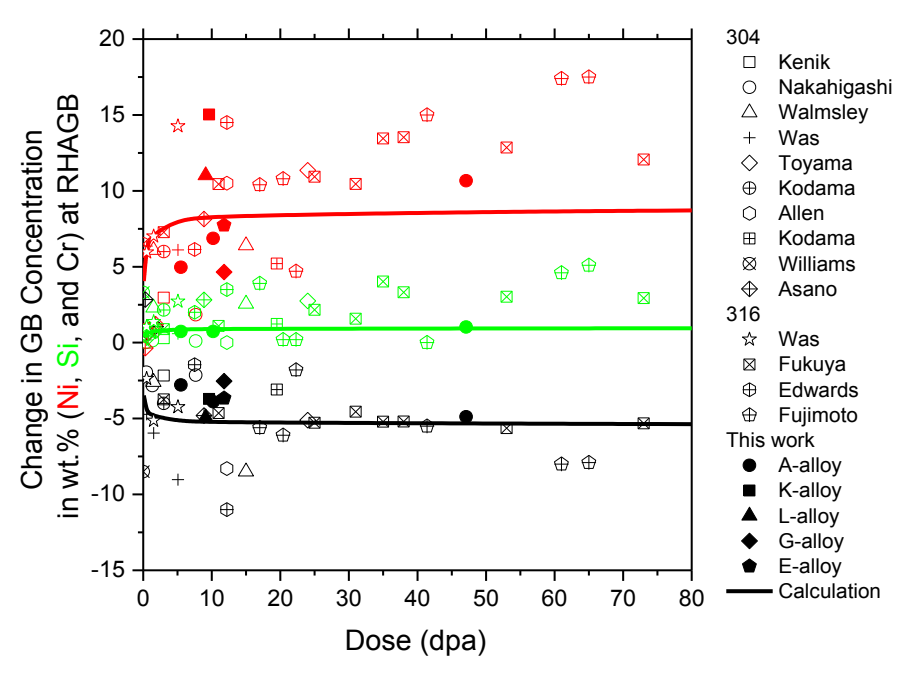


Fig. 6. Concentration changes of Ni, Si, and Cr at random high-angle GBs in investigated alloys (in solid symbols) compared with results reported in the literature and calculated results (in lines).

Based on the high degree of overlap between the values reported here and those in literature, some key conclusions can be drawn. This study highlights that the most dramatic effect of altering the RIS response is not composition or dose but the GB structure (identified by type). This effect has been studied by several authors 11,13,41,42,43,44,45,46,47 and can be attributed to how the mobile point defects and defect clusters are annihilated or absorbed at GBs under irradiation. Based on the calculated concentration of vacancies and interstitials as a function of distance from the defect sink and as a function of irradiation time, RIS modeling shows the RHAGB

continuously behaves like a perfect sink, so that the defect concentration is maintained at thermal equilibrium. With the modified GB condition, the defect concentrations at a $\Sigma 3$ boundary accumulate first and then reach a steady state. The steady state defect concentration at $\Sigma 3$ GBs is reached very early in the irradiation for the conditions assumed here (on the order of 10 s or $\sim 8 \times 10^{-6}$ dpa). The accumulation of defects transported from the bulk in the $\Sigma 3$ GB under sink steady state conditions leads to smaller concentration gradients of defects compared with those in the RHAGB. The smaller concentration gradient of defects at the $\Sigma 3$ GB leads to a smaller driving force for the diffusion flux of all elements to the GBs and therefore less segregation of elements.

As silicon RIS can be quite dramatic in 304 and 316 SS and is expected to play a critical role in the growth of the γ' phase, we also undertook to model silicon RIS from ab initio energetics. Such models help overcome the limitations of fitting atomic-scale thermodynamic and kinetic parameters to existing experimental RIS and related thermokinetics data. Such fits typically have limited data at relevant temperatures as a result of slow kinetics, and a lack of interstitial data because of the difficulty of producing them thermally, and they cannot robustly determine all the possibly relevant atomic-scale parameters. These limitations can lead to inaccuracies when the model is extrapolated to new conditions not used in the fitting. The results of the ab initio modeling show that both vacancies and interstitials contribute significantly to the silicon RIS. The importance of vacancies to the RIS was unexpected, as silicon enrichment is generally attributed to interstitial effects and vacancies are assumed to play no role or to lead to silicon depletion. However, our results show that the vacancy drag helps enrich the silicon at sinks under irradiation in austenitic systems. These results will be used to improve the GiMIK model, which presently assumes just an interstitial contribution.

Phase Stability

Phase instability and formation of secondary phases (both radiation-induced and radiation-enhanced) may compromise material performance. As LWRs age, phase instability may become a phenomenon of increasing importance. Radiation-induced phase transformation, e.g., ferrite formation, was observed in some of the samples in Table 1. 48,49 It was shown that the amount of ferrite may reach a few percent at 10–15 dpa. Silicon and manganese increased the ferrite formation rate, and carbon and molybdenum resisted ferrite accumulation. Although the amount of ferrite was found to saturate at ~10–12 dpa, 49 variations in irradiation temperature, neutron spectra, and other factors may greatly promote it. Ferrite formation can be nondestructively detected by measuring magnetic properties, which may be correlated with IASCC susceptibility because of the observed correlation between magnetic flux density and IASCC susceptibility. Magnetic phases (ferrite and/or martensite) have been observed in neutron-irradiated 304SS and 316SS at lower strain levels than in unirradiated samples. The easily produced magnetic phases which may aggravate IASCC susceptibility.

The observed radiation-induced new phases include a cubic-on-cubic G-phase and a random unknown phase in most of the analyzed samples, together with a cubic-on-cubic γ' -phase only in alloy B favored by its high silicon content. Unlike the G-phase preferentially observed at the interface between voids and austenitic SS matrix because of RIS at the interface during the irradiation to 11 dpa at 500°C,⁵ the favorable formation sites of radiation-induced G-phase, γ' -phase and the unknown phase were not identified in this work. Grain boundaries with such high levels of RIS of Ni and Si were free of G-phase and γ' -phase. The average sizes and densities of the observed phases were analyzed, leading to the estimated volume fractions of the precipitates

assuming a spherical shape. Figure 7 plots the dose-dependent size, density, and volume fraction (vol %) of the precipitates characterized in this work (solid symbols) and reported in the same literature illustrated in Fig. 1. The alloy samples were irradiated to 5.5–120 dpa at 320–343°C. For the G-phase, increasing the dose led to a slight size increase (\sim 3–9 nm) and density reduction (primarily from 10^{22} to 10^{21} m⁻³). The size and density combination led to a quick increase to \sim 0.7 vol % at small doses ($<\sim$ 20 dpa) and then a decrease to relatively stable volume fractions (\sim 0.03–0.1 vol %). The limited data for the γ' -phase exhibit a similar dose dependence. The G-phase generally exhibits larger sizes, comparable densities, and larger volume fractions than the γ' -phase. The dose dependence of the unknown phase is not clear because of the limited data.

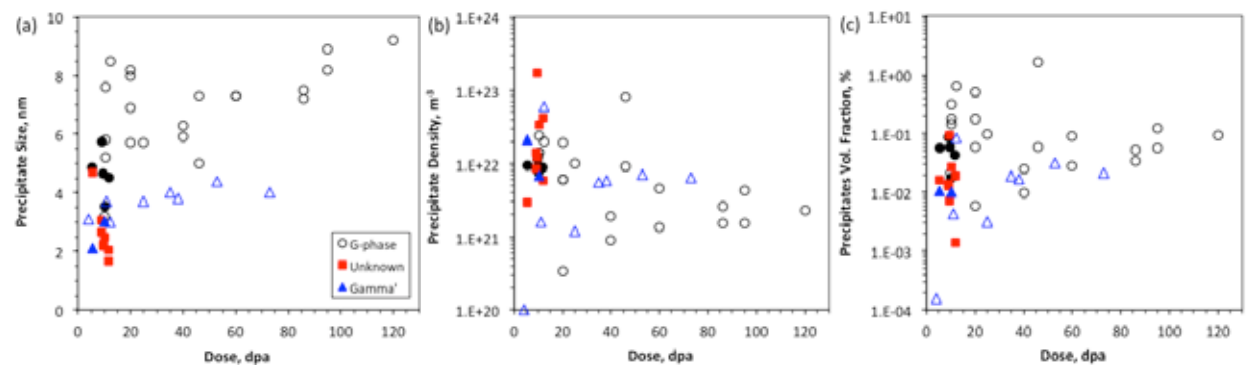


Fig. 7. Dose-dependent precipitate (a) size, (b) density, and (c) volume fraction of the G-phase (circles), unknown phase (filled squares), and γ' (triangles) observed in this work (solid symbols) and literature reports (open symbols).

Figure 8 shows results from the MatCalc model predictions of second-phase precipitate evolution at 400°C in a 316 austenitic SS with a modified composition to account for the effects of RIS typically observed in LWR irradiation at a dose of about 10 dpa. It also incorporates the impact of increased diffusion coefficients for either Cr and Ni (Fig. 8a) or Cr, Ni, Mn and Si (Fig. 8b). In this case, the steel corresponding to RIS had an assumed composition of Fe-12%Cr-21%Ni-1%Mo-1%Mn-5%Si-0.05%C-0.03%N, and effectively had greatly increased nickel and silicon concentrations and a decreased chromium concentration. As shown in Fig. 8, the model predicts that significant concentrations of the γ' and G phases will develop within about 104 hours at 400°C, and that the formation kinetics will be greatly accelerated if manganese and silicon, in addition to chromium and nickel, experience radiation-enhanced diffusion. The silicon content appears to play a crucial role in the formation of the γ' and G phases. Although the γ' phase is dominant over the G-phase for typical compositions of 316 austenitic SS, it appears that G-phase should be the major radiation-induced precipitate in titanium-stabilized austenitic SS. Although not shown here, it was found that an increase in dislocation density, as is observed to occur in irradiated SS, significantly enhances the precipitation kinetics of the γ' and G phases, as well as M₂₃C₆ and M₆C. ¹⁹ Further, increases in the diffusivity of manganese and silicon, as expected owing to radiation-enhanced diffusion, drastically accelerate the precipitation kinetics of both phases, even more so than increases in the chromium or nickel diffusivities. The predicted average precipitate size of the radiation-induced precipitates is in reasonable agreement with experimental observations in the literature. In general, the results in Fig. 8 are within the range of the experimental data reported in Fig. 7, although clearly future effort is required to

more explicitly couple the spatial dependence of the radiation-induced effects to the modified thermokinetics.

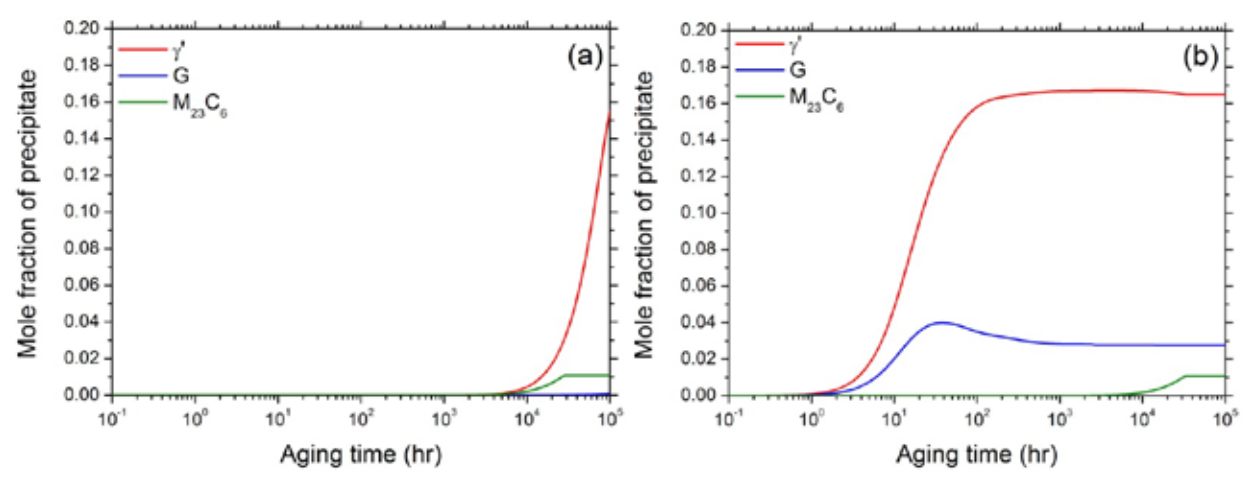


Fig. 8. Simulated precipitate evolution in a 316SS as a function of aging time at 400°C, assuming a modified composition consistent with GB segregation following 10 dpa irradiation (Fe-12%Cr-21%Ni-1%Mo-1%Mn-5%Si-0.05%C-0.03%N) and incorporating an increased diffusivity associated with radiation-enhanced diffusion for (a) only Cr and Ni or (b) Cr, Ni, Mn and Si.

Radiation Hardening

Radiation hardening was usually directly assessed by hardness measurements and/or tensile tests of miniature specimens at room temperature and/or the irradiation temperatures. These tests were usually conducted in hot cells or dedicated facilities, depending on the activities of the irradiated specimens, which limits the availability of the experimental data. Meanwhile, estimation of radiation hardening using the dispersed barrier-hardening model of $\Delta \sigma_v \approx$ $M\alpha\mu b\sqrt{Nd}$ has been broadly pursued, where M is the Taylor factor (3.06 for face-centered cubic polycrystals⁵²), α the strength factor, μ the shear modulus of the matrix, b the magnitude of the Burgers vector of the moving dislocation, and N and d number density and size of discrete obstacles, respectively. Recently, the strength factors of Frank loops, precipitates, and cavities were deduced and simplified to a format of $\alpha = k_1 \ln(k_2 d)$, with k_1 and k_2 as the fitting parameters.⁵³ Radiation hardening of the alloy samples investigated in this work was estimated using the calculated α and characterized d and N, which are in good agreement with the experimentally measured hardening, as shown in Fig. 9a. The radiation to 4.4–11.8 dpa at 320°C resulted in about 500-1,000 MPa hardening. It seems that cold-working of alloys B, E, F, and G noticeably reduced their hardening compared with the solution annealing of alloys A, P, and SW. Additionally, alloys with higher SFEs tend to have lower hardening, as shown in Fig. 9b. This is consistent with the effect of SFE on loop density, suggesting Frank loops as a significant component of hardening.

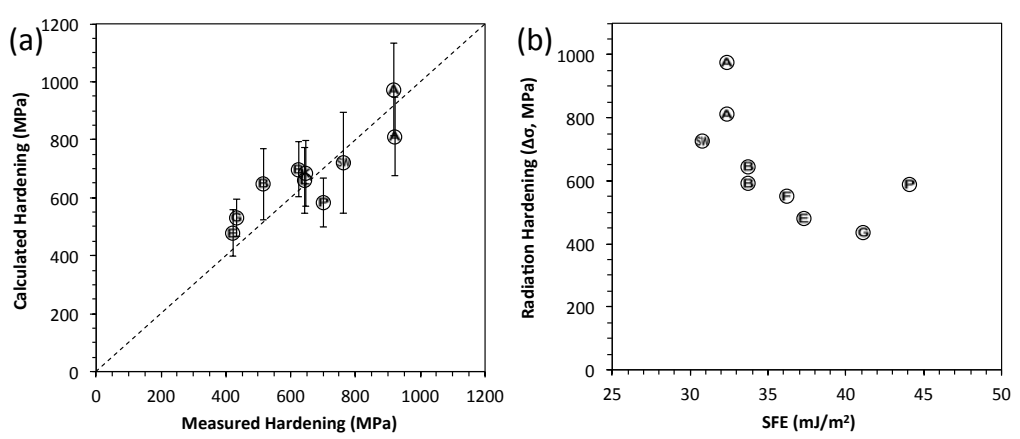


Fig. 9. (a) Comparison of measured and calculated radiation hardening and (b) SFE-dependence of radiation hardening in the analyzed alloy samples.

CONCLUSION

Type 304 and 316 SS are primary internal-core structural materials in LWRs. Extending the lives of LWRs will pose significant challenges to the materials, and radiation damage is one of the primary concerns. Microstructural evolutions including Frank loops, cavities, precipitates, and segregation at boundaries are reviewed in this paper based on the data collected in this work and from literature reports—which include up to 40 heats of type 304 and 316 variants irradiated in BOR-60, LWRs, and experimental reactors to 0.6-120 dpa at 275-375°C. Frank loops have average sizes primarily in the range of $\sim 5.7-12.5$ nm and densities on the order of 10^{22} to 10^{23} m ³. A slight dose-dependence exists for average loop size and density. Primarily G-phase (up to ~ 0.7 vol %) with some γ '-phase (up to ~ 0.08 vol %, only in type 316SS variants with high silicon content) and an unknown phase (up to ~0.09 vol %) were observed in the irradiated samples. Cavities were primarily reported in cold-worked 316SS at sizes of ~0.5-2 nm and densities on the order of 10^{23} m⁻³, which resulted in swelling (up to $\sim 0.07\%$) increasing with the dose (up to 73 dpa). Cavities were also observed in solution-annealed 304SS at slightly larger sizes and smaller densities but comparable swelling, compared with cold-worked 316SS. A few data in terms of sizes, densities, and volume fractions deviated from the common trends; they may be attributable to the complex combinatorial influences of irradiation temperatures, doses, dose rates, alloy compositions and conditions, as well as experimental errors. The radiationinduced microstructural evolution resulted in hardening in the type 304SS and 316SS variants by ~500–1,000 MPa, which was successfully estimated using the dispersed barrier-hardening model with the formatted strength factor. Alloys with cold work or higher SFE tend to have smaller radiation hardening.

The Frank loop and dislocation simulation suggested the dose dependence of the predicted loop density appears to be stronger, and the initial recovery of the dislocation network begins to be compensated for, when the largest loops unfaulted and become part of the network at about 1 dpa. The cavity simulation shows the effect of irradiation temperature on swelling is weak in the range of 275–300°C. The results suggest that it may be reasonable to expect a tendency for this type of materials to swell even at these relatively low temperatures.

RIS was found to be strongly dependent on several factors, including alloy composition, irradiation dose, and GB structure; the latter had the strongest ability to suppress segregation to

GBs under irradiation. A rate theory model developed from the MIK model corroborates these results and provides detailed insight into the confluence between radiation-induced point defects, solute species, and defect sinks in irradiated 304/316SS. Additional insight into silicon RIS was provided by ab initio calculation. It suggested the silicon RIS can be affected by both interstitial diffusion and vacancy drag. Therefore, additional work may be needed to refine the GiMIK models for silicon diffusion.

The precipitation modeling provides a crude, initial approximation of the effects of radiation in the absence of coupled defect evolution physics and thermokinetic models; but it can shed light on important mechanisms that may dominate the aging evolution of austenitic SS components during extended LWR irradiation.

ACKNOWLEDGMENT

This research was sponsored by the US Department of Energy, Office of Nuclear Energy, Light Water Reactor Sustainability Program, under contract DE-AC05-00OR22725 with University of Tennessee–Battelle, LLC. The United States Government retains and the publisher, by accepting the article for publication, acknowledges that the United States Government retains a non-exclusive, paid-up, irrevocable, world-wide license to publish or reproduce the published form of this manuscript, or allow others to do so, for United States Government purposes. The Department of Energy will provide public access to these results of federally sponsored research in accordance with the DOE Public Access Plan (http://energy.gov/downloads/doe-public-access-plan).

REFERENCES

1. K. Fukuya, J. Nucl. Sci. Tech. 50, 213 (2013).

^{2.} T.R. Allen and J.T. Busby, *JOM* 61, 29 (2009).

^{3.} E.A. Kenik and J.T. Busby, *Mater. Sci. Eng. R* 73, 67 (2012).

^{4.} S.J. Zinkle and G.S. Was, Acta Mater. 61, 735 (2013).

^{5.} F.A. Garner, Radiation damage in austenitic steels, in: R.J.M. Konings, T.R. Allen, R.E. Stoller, S. Yamanaka (Eds.), Comprehensive Nuclear Materials, Elsevier, 2012.

^{6.} CIR II program: Description of the Boris 6 and 7 experiments in the BOR-60 fast breeder reactor, EPRI, Palo Alto, CA: 2005. 1011787.

^{7.} R.E. Stoller and G.R. Odette, "A Composite Model of Microstructural Evolution in Austenitic Stainless Steel Under Fast Neutron Irradiation," Radiation Induced Changes in Microstructure: 13th International Symposium, ASTM STP 955, F.A. Garner, N.H. Packan, and A.S. Kumar, eds., American Society for Testing and Materials, Philadelphia, 1987, pp. 371–392.

^{8.} R.E. Stoller, A.V. Barashev, and S.I. Golubov, Cavity nucleation under irradiation conditions typical of LWR internal components, ORNL/LTR-2013/487, Oak Ridge National Laboratory, May 2013.

^{9.} S.I. Golubov, A.M. Ovcharenko, A.V. Barashev, and B.N. Singh, *Philos. Mag. A* 81, 643 (2001).

^{10.} S.I. Golubov, R.E. Stoller, and S.J. Zinkle, Nucleation and growth of helium-vacancy clusters in irradiated metals. Part. I. A group method for an approximate solution of two

dimensional kinetic equations describing evolution of point defect clusters, Fusion Reactor Materials, Semi-annual progress report for period ending December 31, 2002, DOE/ER-0313/33, US Department of Energy, pp. 155–180.

- 11. K.G. Field, Y. Yang, T.R. Allen, and J.T. Busby, *Acta Mater.* 89, 438 (2015).
- 12. T.R. Allen, J.T. Busby, G.S. Was, and E.A. Kenik, J. Nucl. Mater. 255, 44 (1998).
- 13. T.S. Duh, J.J. Kai, and F.R. Chen, J. Nucl. Mater. 283–287, 198 (2000).
- 14. N.Q. Lam, J. Nucl. Mater. 117, 106 (1983).
- 15. H. Wiedersich, P.R. Okamoto, and N.Q. Lam, J. Nucl. Mater. 83, 98 (1979).
- 16. J.D. Tucker, R. Najafabadi, T.R. Allen, and D. Morgan, J. Nucl. Mater. 405, 216 (2010).
- 17. E. Kozeschnik, J. Svoboda, P. Fratzl, and F.D. Fischer, Mater. Sci. Eng. A 385, 157 (2004).
- 18. E. Kozeschnik, J. Svoboda, and F.D. Fischer, CALPHAD 28, 379 (2004).
- 19. J.S. Shim, E. Povoden-Karadeniz, E. Kozeshnik, and B.D. Wirth, *J. Nucl. Mater.* 462, 250 (2015).
- 20. J. Svoboda, F.D. Fischer, P. Fratzl, and E. Kozeschnik, *Mater. Sci. Eng. A* 385, 166 (2004).
- 21. http://www.matcalc.com
- 22. T. Tokunaga, K. Hashima, H. Ohtani, and M. Hasebe, Mater. Trans. 45, 1507 (2004).
- 23. B. Hu, H. Xu, S. Liu, Y. Du, C. He, C. Sha, D. Zhao, and Y. Peng, *CALPHAD* 35, 346 (2011).
- 24. R.L. Simons and L.A. Hulbert, "Correlation of yield strength with irradiation-induced microstructure in AISI type 316 stainless steel," in: F.A. Garner, J.S. Perrin (eds.), *Effects of Radiation on Materials: 12th Int. Symp.*, ASTM STP 870, 1985, pp. 820–839.
- 25. L. Tan, J.T. Busby, H.J.M. Chichester, K. Sridharan, and T.R. Allen, *J. Nucl. Mater.* 437, 70 (2013).
- 26. D.J. Edwards, E.P. Simonen, and S.M. Bruemmer, J. Nucl. Mater. 317, 13 (2003).
- 27. D.J. Edwards, E.P. Simonen, F.A. Garner, L.R. Greenwood, B.M. Oliver, and S.M. Bruemmer, *J. Nucl. Mater.* 317, 32 (2003).
- 28. D.J. Edwards, F.A. Garner, S.M. Bruemmer, and Päl Efsing, J. Nucl. Mater. 384, 249 (2009).
- 29. D.J. Edwards, A. Schemer-Kohrn, and S. Bruemmer, "Characterization of neutron-irradiated 300-series stainless steels," EPRI, Palo Alto, CA: 2006. 1009896
- 30. D.J. Edwards and S.M. Bruemmer, Characterization of CIR II irradiated stainless steels, EPRI, Palo Alto, CA: 2008. EP-P19021/C9406
- 31. Y. Yang, Y. Chen, Y. Huang, T. Allen, and A. Rao, Irradiation microstructure of austenitic steels and cast steels irradiated in the BOR-60 reactor at 320°C, in: J.T. Busby, G. Ilevbare, P.L. Andresen (Eds.), 15th Int. Conf. on Environmental Degradation of Materials in Nuclear Power Systems-Water Reactors, John Wiley & Sons, Inc., 2012, pp. 2137–2148.
- 32. Y. Yang, T.R. Allen, Y. Chen, and O.K. Chopra, Dose dependence of radiation hardening of austenitic steels in Bor-60 at PWR-relevant temperatures, 14th Int. Conf. on Environmental Degradation of Materials in Nuclear Power Systems, Virginia Beach, VA, US, August 23–27, 2009, pp. 1335-1340.
- 33. A.-É. Renault, C. Pokor, J. Garnier, and J. Malaplate, Microstructure and grain boundary chemistry evolution in austenitic stainless steels irradiated in the BOR-60 reactor up to 120 dpa, ibid., pp. 1324–1334.
- 34. Y. Chen, O.K. Chopra, W.K. Soppet, W.J. Shack, Y. Yang, T. Allen, and A.S. Rao, Cracking behavior and microstructure of austenitic stainless steels and alloy 690 irradiated in BOR-60 reactor, phase I, Argonne National Laboratory, ANL/09-32

- 35. C. Pokor, Y. Brechet, P. Dubuisson, J.-P. Massoud, and A. Barbu, *J. Nucl. Mater.* 326, 19 (2004).
- 36. K. Fukuya, K. Fuji, H. Nishioka, and Y. Kitsunai, J. Nucl. Sci. Tech. 43, 159 (2006).
- 37. T. Yonezawa, K. Suzuki, S. Ooki, and A. Hashimoto, *Metall. Mater. Trans. A* 44, 5884 (2013).
- 38. Materials reliability program characterization of type 316 cold-worked stainless steel highly irradiated under PWR operating conditions (MRP-73), EPRI-1003525, August, 2002.
- 39. P. Doig, D. Lonsdale, and P.E.J. Flewitt, *Phil. Mag. A* 41, 761 (1980).
- 40. P. Doig, D. Lonsdale, and P.E.J. Flewitt, Quantitative microanalysis with high spatial resolution, The Metals Society, London, 1981.
- 41. T.S. Duh, J.J. Kai, F.R. Chen, and L.H. Wang, J. Nucl. Mater. 294, 267 (2001).
- 42. R. Hu, G.D.W. Smith, and E.A. Marquis, *Acta Mater.* 61, 3490 (2013).
- 43. C.M. Barr, G.A. Vetterick, K.A. Unocic, K. Hattar, X.-M. Bai, and M.L. Taheri, *Acta Mater*. 67, 145 (2014).
- 44. G.-G. Lee, H.-H. Jin, Y.-B. Lee, and J. Kwon, J. Nucl. Mater. 449, 234 (2014).
- 45. M. Tomozawa, Y. Miyahara, and K. Kako, *Mater. Sci. Eng. A* 578, 167 (2013).
- 46. K.G. Field, L.M. Barnard, C.M. Parish, J.T. Busby, D. Morgan, and T.R. Allen, *J. Nucl. Mater.* 435, 172 (2013).
- 47. K.G. Field, B.D. Miller, H.J.M. Chichester, K. Sridharan, and T.R. Allen, *J. Nucl. Mater.* 445, 143 (2014).
- 48. L. Tan and J.T. Busby, *J. Nucl. Mater.* 443, 351 (2013).
- 49. M.N. Gussev, J.T. Busby, L. Tan, and F.A. Garner, J. Nucl. Mater. 448, 294 (2014).
- 50. S. Takaya, Y. Nagae, T. Yoshitake, Y. Nemoto, J. Nakano, F. Yeno, K. Aoto, and T. Tsukada, *E-J. Adv. Maintenance* 1, 44 (2009).
- 51. M.N. Gussev, K.G. Field, and J.T. Busby, J. Nucl. Mater. 446, 187 (2014).
- 52. R.E. Stoller and S.J. Zinkle, *J. Nucl. Mater.* 283–287, 349 (2000).
- 53. L. Tan and J.T. Busby, *J. Nucl. Mater.* 465, 724 (2015).